

In-orbit background and sky survey simulation study of POLAR-2/LPD

ZU-KE FENG,¹ HONG-BANG LIU,¹ FEI XIE,¹ HUAN-BO FENG,¹ QIAN-NAN MAI,¹ JIANG-CHUAN TUO,¹ QIAN ZHONG,¹
JIAN-CHAO SUN,² JIANG HE,² YUAN-HAO WANG,² QIAN LIU,³ DI-FAN YI,³ RUI-TING MA,³ BIN-LONG WANG,³
ZHEN-YU TANG,⁴ SHUANG-NAN ZHANG,² AND EN-WEI LIANG¹

¹*School of Physical Science and Technology, Guangxi University, Nanning 530004, China*

²*Key Laboratory of Particle Astrophysics, Institute of High Energy Physics, Chinese Academy of Sciences, Beijing 100049, China*

³*School of Physics Science, University of Chinese Academy of Sciences, Beijing, 100049, China*

⁴*Beijing Institute of Spacecraft Environment Engineering, Beijing 100094, China*

ABSTRACT

The Low-Energy X-ray Polarization Detector (LPD) is one of the payloads in the POLAR-2 experiment, designed as an external payload for the China Space Station (CSS) deployment in early 2026. LPD is specifically designed to observe the polarization of Gamma-Ray Bursts (GRBs) prompt emission in the energy range of 2-10 keV, with a wide field of view (FoV) of 90 degrees in preliminary design. This observation is achieved using an array of X-ray photoelectric polarimeters based on gas pixel detectors. Due to the wide FoV configuration, the in-orbit background count rate in the soft X-ray range is high, while GRBs themselves also exhibit a high flux in this energy band. In order to assess the contribution of various background components to the total count rate, we conducted detailed simulations using the GEANT4 C++ package. Our simulations encompassed the main interactions within the instrument materials and provided insights into various background components within the wide FoV scheme. The simulation results reveal that among the background components, the primary contributors are the cosmic X-ray background (CXB) and bright X-ray sources. The total background count rate of LPD, after applying the charged particle background rejection algorithm, is approximately 0.55 counts/cm²/s on average, and it varies with the detector's orbit and pointing direction. Furthermore, we performed comprehensive simulations and comparative analyses of the CXB and X-ray bright sources under different FoVs and detector pointings. These analyses provide valuable insights into the background characteristics for soft X-ray polarimeter with wide FoV.

Keywords: Gamma-ray bursts (629)

1. INTRODUCTION

Over the past few decades, there has been a growing interest in the detection of polarization in X-ray and gamma-ray astronomy, particularly for the study of one of the most powerful cosmic events: GRBs. Satellites like Swift (Burrows et al. 2005) and Fermi (Atwood et al. 2009) have significantly advanced our understanding of GRBs by providing valuable observations of their energy spectra and timing properties, both during the prompt emission phase and the subsequent afterglow. Despite these advancements, several fundamental questions regarding the nature of GRBs remain unanswered, including the properties of the central engine, the mechanisms driving the energetic jets, the composition of the jets, the processes responsible for energy dissipation, the configurations of magnetic fields, and the mechanisms behind particle acceleration and radiation (Kumar & Zhang 2015; Narayan & Kumar 2009; Lundman et al. 2012; Narayan & Kumar 2009; Zalamea & Beloborodov 2011; Zhang & Mészáros 2002; Bégué & Burgess 2016; Rees & Meszaros 1994).

In contrast, the polarization of photons provides crucial insights into the magnetic field structures, angular structures of the jets, and emission mechanisms within the GRB emission region (Toma et al. 2009; Gill et al. 2020, 2021; Gill & Granot 2021; Lundman et al. 2014; Lazzati et al. 2004; Granot & Königl 2003). By studying the polarization

properties, we can gain a deeper understanding of the physical processes occurring in the vicinity of the central engine and the mechanisms responsible for the explosive release of energy during a GRB.

The study of gamma-ray burst (GRB) polarization has been conducted using the principle of Compton scattering by several missions, including RHESSI (150 keV to 2 MeV) (Coburn & Boggs 2003), INTEGRAL-IBIS (250 keV to 800 keV) (Götz et al. 2013), INTEGRAL-SPI (100 keV to 350 keV) (Kalemci et al. 2007), IKAROS-GAP (50 keV to 300 keV) (Yonetoku et al. 2012), AstroSat-CZTI (100 keV to 300 keV) (Vadawale et al. 2015), COSI (200 keV to 5 MeV) (Lowell et al. 2017), and POLAR (50 keV to 500 keV) (Zhang et al. 2019). Additionally, there are planned missions specifically designed for GRB detection, such as LEAP (30 keV to 500 keV) (McConnell et al. 2021). However, these instruments operate in the hard X-ray or gamma-ray range, leaving the soft X-ray polarization observation of GRBs largely unexplored.

Theoretical studies suggest a correlation between the predicted polarization degree of different polarization models and the observed energy range. For instance, synchrotron radiation and Compton drag models predict lower polarization degrees at lower energy ranges (Toma et al. 2009), while the polarization from the photosphere model becomes more significant around several keV (Lundman et al. 2018). The Low-Energy X-ray Polarization Detector (LPD) aims to fill this gap by employing an array of photoelectric polarimeters with a wide FoV to achieve polarization detection of GRBs in the 2-10 keV energy range. Although projects like IXPE and eXTP also utilize similar techniques optimized for the soft energy range, they primarily focus on persistent point sources during long exposures and virtually impossible to detect GRB prompt emission, due to the narrow FoV caused by the focusing optics, and with slower reorientation. It is worth mentioning that, IXPE has reported polarimetric observations of the afterglow from the brightest GRB recorded to date, GRB221009A, providing valuable insights into its properties (Negro et al. 2023). Additionally, due to the limited effective area of CubeSat platforms such as PolarLight, the number of collected photons is limited, making it challenging to achieve high-sensitivity polarization detection of GRBs.

The standard parameter used to quantify the sensitivity to polarization is the Minimum Detectable Polarization (MDP) at a confidence level of 99%. It is defined as (Weisskopf et al. 2010):

$$MDP_{99} = \frac{4.29}{\mu S} \sqrt{\frac{S+B}{T}} \quad (1)$$

Where S and B are the count rate of the source and background, T is the total exposure time and μ is the modulation factor representing the amplitude of the response to 100% polarized beam. In the case of GRBs prompt emission, they often exhibit high flux in the soft X-ray range. However, it is crucial to understand and mitigate the background count rate, which is also high in this energy range due to the wide FoV of the instrument. To address this, a detailed mass model of the LPD has been developed, as shown in Fig. 7, and simulations of the primary interactions within the instrument materials have been performed using the Geant4 framework (Agostinelli et al. 2003; Allison et al. 2006). These simulations allow for the analysis and characterization of the main background components that deposit energy in the sensitive regions of the working gas, considering the wide FoV scheme. The simulation results highlight that the main background sources are the cosmic X-ray background (CXB) and bright X-ray sources. To gain a better understanding of these background components, we conducted detailed simulations and performed comparative analysis under different FoVs and different pointings of the detector.

This paper is organized as follows: In Section 2, we provide an introduction to the POLAR-2 mission and the LPD payload. Section 3 focuses on the background characterization. We present the input spectrum of various background components and describe the simulated results. Additionally, we discuss the algorithm used for background rejection, specifically targeting charged particles. In Section 4, we delve into the X-ray sources catalogue and simulated sky survey. We describe the methodology and techniques employed to create the catalogue, which includes a comprehensive survey of X-ray sources. This section provides essential information about the sources considered in the analysis and their impact on the overall observations. Finally, Section 5 presents a summary of this work and a comprehensive discussion.

2. THE POLAR-2 MISSION AND LPD

POLAR-2 is the successor of the POLAR experiment (Produit et al. 2018) and will be deployed as an external payload on the CSS in 2026. It consists of three detectors: a high-energy polarization detector (HPD) covering 30-800 keV developed by Europe (Hulsman 2020), a low-energy polarization detector (LPD) covering 2-10 keV developed by China, and a broad-spectrum detector (BSD) covering 8-2000 keV developed by China. In addition to the significant

Table 1. The main performance parameters of LPD.

Parameters	Anticipated value
Energy range	2-10 keV
Window	50 μm Be
Gas mixture	Ne 30% + DME 70% at 0.8 atm
Absorption depth	1.36 cm
Detection area	$\sim 298 \text{ cm}^2$
FoV	$\sim 90^\circ \times 90^\circ$
Energy resolution (FWHM)	$\leq 20 \%$ @ 5.9 keV $\sim 7.8\%$ @GRB190114C* $\sim 10.3\%$ @GRB191019A $\sim 10.6\%$ @GRB210619B $\sim 18.7\%$ @GRB201216C $\sim 23.1\%$ @GRB210822A $\sim 26.2\%$ @GRB210818A $\sim 30.1\%$ @GRB201026A
Minimum Detectable Polarization (MDP) for a 20-degree oblique incidence	

* The fluences of these GRBs at 15-150 keV are (data from official website of Swift/BAT^a, unit: erg/cm^2): $8.26 \times 10^{-5} \pm 9.57 \times 10^{-7}$ @GRB190114C, $1.04 \times 10^{-5} \pm 2.59 \times 10^{-7}$ @GRB191019A, $9.49 \times 10^{-5} \pm 1.07 \times 10^{-6}$ @GRB210619B, $4.51 \times 10^{-5} \pm 7.30 \times 10^{-7}$ @GRB201216C, $1.99 \times 10^{-5} \pm 3.84 \times 10^{-7}$ @GRB210822A, $2.62 \times 10^{-5} \pm 3.37 \times 10^{-7}$ @GRB210818A, $5.63 \times 10^{-6} \pm 2.43 \times 10^{-7}$ @GRB201026A.

^a <https://www.swift.ac.uk/>

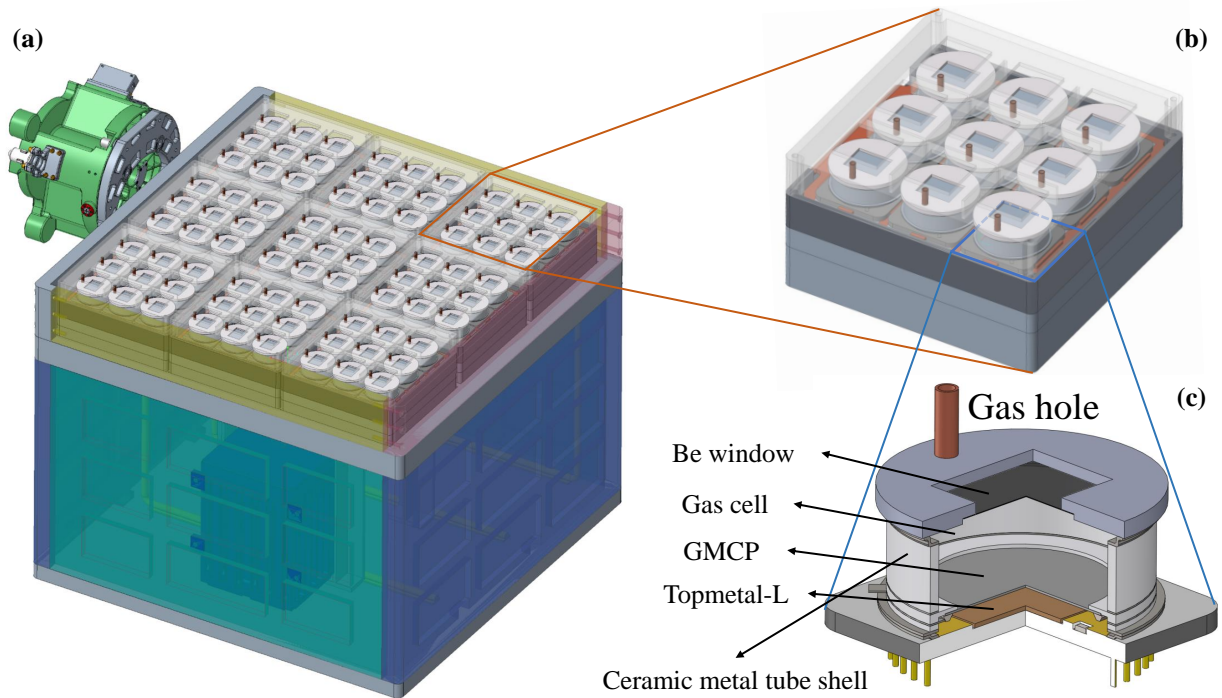


Figure 1. Mechanical structures of LPD. (a) The LPD payload. (b) The detector array module. Each module includes a 3x3 array of detector units. (c) The detector unit. The main components of the gas chamber have been indicated in the diagram. Additionally, the material of the top cover is Kovar, the material of the gas hole is copper, the chamber walls are made of alumina ceramic, and the bottom consists of a ceramic base.

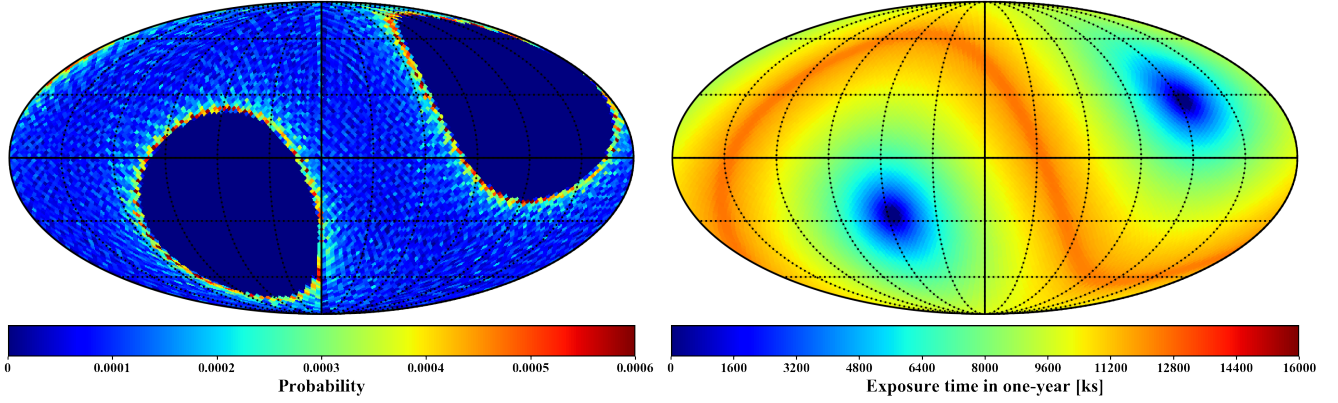


Figure 2. Left panel: Distribution of pointing directions in Galactic coordinates during a one-year simulation. The color indicates the normalized probability of pointing in each direction (total 12288 pixels). Right panel: Distribution of exposure time during a one-year simulation.

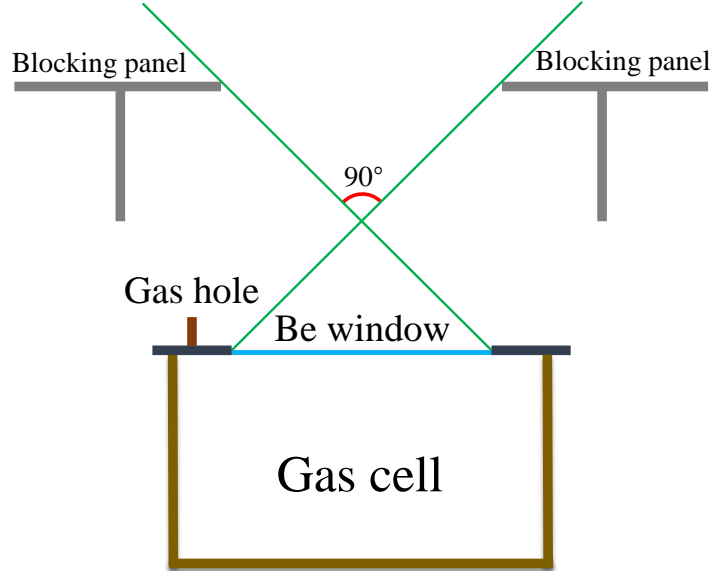


Figure 3. Definition of FoV. The diagram provides an example of defining the FoV size using a 90-degree FoV, as indicated by the green line.

improvement in the detection ability of high-energy polarization, it also has capabilities of soft X-ray polarization measurement, wide energy spectrum measurement, timing measurement and location.

LPD is an innovative soft X-ray polarization detector with a wide FoV (the definition of FoV is shown in Fig. 3), utilizing the Gas Microchannel Plate pixel Detector (GMCP) array (Feng et al. 2023a,b; Xie et al. 2023). It was proposed by Guangxi University in China. The performance and key parameters of LPD are summarized in Table 1, showcasing its anticipated capabilities and characteristics.

2.1. Geometric structure

LPD is comprised of a total of 9 detector modules arranged in a 3×3 array configuration. Each detector module contains 9 detector units, resulting in a total of 81 detector units. Each unit consists of a cathode, Gas Microchannel Plate (GMCP), pixel readout chip (Topmetal-L), and a gas-sealed chamber, as illustrated in Fig. 1 (c). The GMCP serves as the electron multiplying device, while the Topmetal-L, manufactured using the CMOS process, acts as the readout chip responsible for measuring the tracks of photoelectrons and deriving the polarization information of the incident X-ray. Topmetal-L represents an upgraded version of Topmetal-II (Li et al. 2021; Fan et al. 2023), specifically designed for LPD to detect transient sources. It features a smaller pixel size and a larger chip area, measuring 16mm

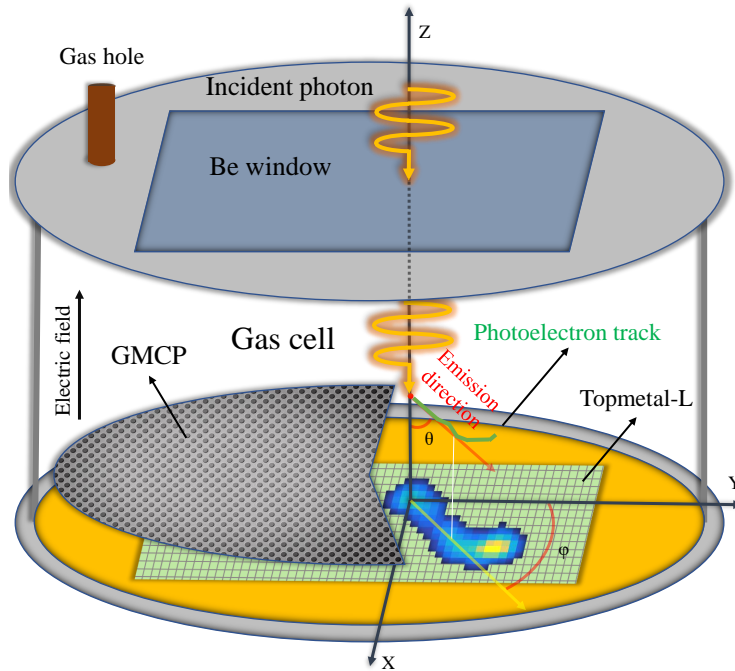


Figure 4. Polarization detection principle of microchannel plate pixel detector. When an X-ray photon penetrates the detector through the beryllium window and interacts with the working gas within the GMPD, photoelectron are emitted. It ionize the gas molecules, generating primary electrons and ions. Guided by the electric field, the primary electrons drift towards the GMCP holes, undergoing an avalanche amplification as they move towards the anode. While some electrons migrate to the top of the silicon pixel chip Topmetal-L, others are collected by the electrodes at the bottom of the GMCP. By reconstructing the emission direction of the photoelectron tracks on Topmetal-L, the polarization of the incident X-ray can be determined. Additionally, information about the X-ray’s energy and time can be extracted by measuring the electrons collected at the bottom of the GMCP.

× 23mm. The LPD unit structure mainly consists of a gas microchannel plate pixel detector and an electronic system. The detector is utilized to measure the photoelectron track, while the readout electronics system controls the detector’s data reading, organization, and packaging. The ceramic-metal sealed chamber of LPD is constructed using a beryllium window, support frame, ceramic-metal tube shell, and ceramic base, all sealed through laser welding. The GMCP and Topmetal-L chip are packaged within the gas chamber. The copper intake tube is used for filling the working gas, which is then sealed using ultrasonic welding.

2.2. Working principle

The microchannel plate pixel detector operates on the same polarization detection principle as the conventional Gas Pixel Detector (GPD), as illustrated in Fig. 4 (Costa et al. 2001). When an X-ray photon penetrates the detector through the beryllium window and interacts with the working gas within the GMPD, photoelectron are emitted. It ionize the gas molecules, generating primary electrons and ions. Guided by the electric field, the primary electrons drift towards the GMCP holes, undergoing an avalanche amplification as they move towards the anode. While some electrons migrate to the top of the silicon pixel chip Topmetal-L, others are collected by the electrodes at the bottom of the GMCP. By reconstructing the emission direction of the photoelectron tracks on Topmetal-L, the polarization of the incident X-ray can be determined. Additionally, information about the X-ray’s energy and time can be extracted by measuring the electrons collected at the bottom of the GMCP.

3. BACKGROUND STUDIES

LPD is expected to be mounted as an external payload on the CSS, always pointing away from the Earth. The orbital altitude of the CSS is approximately 400 km, with an inclination of approximately 42°. Background simulation results from IXPE (Xie et al. 2021) and in-orbit measurement results from Polarlight (Huang et al. 2021a) indicate that gas photoelectric X-ray polarimeters with focusing telescopes or narrow FoV primarily experience background noise from charged particles, including electrons and protons. However, due to LPD’s wide FoV design, the number of

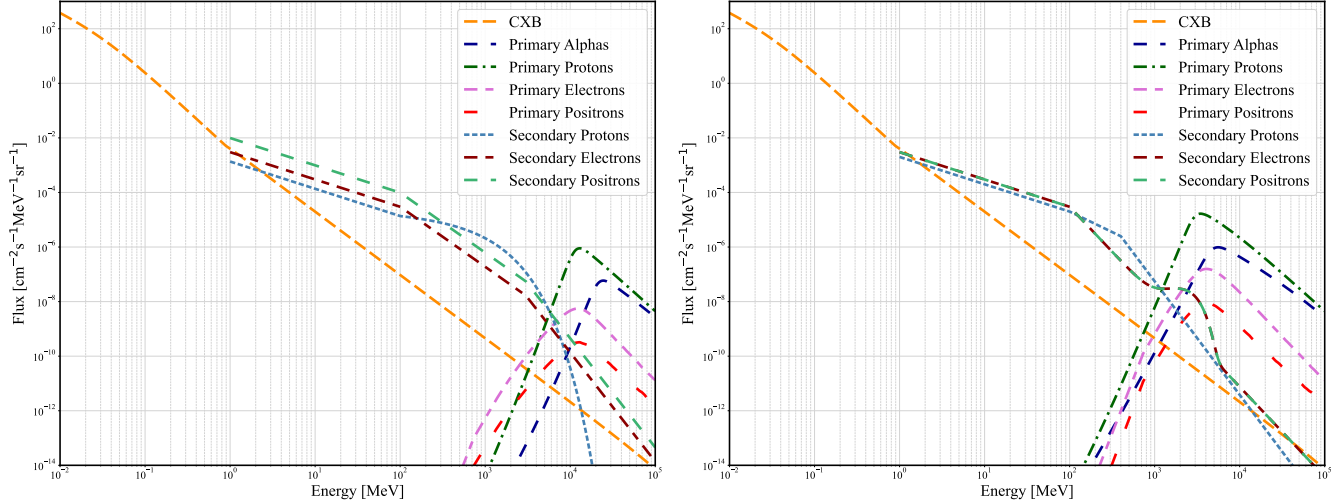


Figure 5. The spectra of main background components expected in the CSS orbital space environment at two magnetic latitudes. (Left panel) 0° . (Right panel) 42° . As shown in the figure, the spectrum of the CXB does not vary with changes in geomagnetic latitude. Additionally, due to the different geomagnetic cut-off rigidities at various geomagnetic latitudes, the cut-off energy of primary charged particles varies significantly.

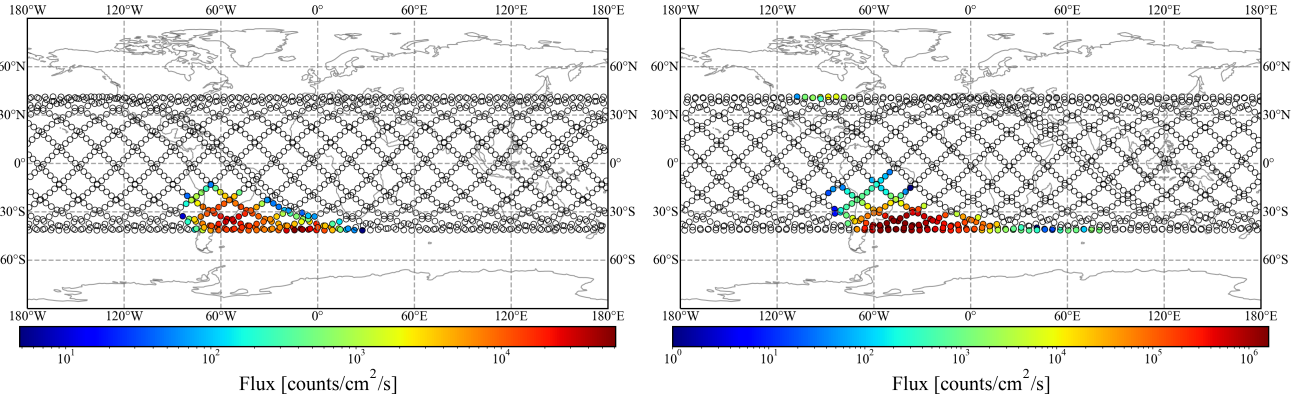


Figure 6. The orbit of the CSS in one day and the flux map of high energy (> 100 keV) charged particles in South Atlantic anomaly and polar regions (solar minimum). Left panel: Proton flux. Right panel: Electron flux (data generated by SPENVIS).

background photons entering the FoV will significantly increase, primarily comprising cosmic X-ray background and X-ray sources with known positions. Taking into account LPD's expected flight orbit and direction away from Earth, the in-orbit backgrounds under the wide FoV scheme mainly consist of the following components: CXB, primary and secondary charged particles, charged particles in the South Atlantic anomaly, and X-ray sources with known positions.

3.1. Space Radiation Environment

The input energy spectrum models of the main background components were obtained from measurements conducted by other missions, as shown in Fig. 5. This figure presents the background energy spectra at two extreme geomagnetic latitudes corresponding to the LPD orbit (Cumani et al. 2019). These spectra include the contributions from CXB, primary and secondary charged particles. Albedo components were not considered in our analysis due to the pointing strategy of POLAR-2.

3.1.1. Cosmic X-ray background

It has been over 50 years since the discovery of the Cosmic X-ray background (Giacconi et al. 1962). Currently, it is understood that the cosmic X-ray emission is attributed to the combined contribution of numerous extragalactic X-ray sources. In the soft X-ray range, the dominant contribution comes from active galactic nuclei, while the origin of some point sources in the hard X-ray range remains uncertain (Giacconi et al. 2001). The intensity of CXB remains

relatively constant over time, and the spatial distribution is isotropic (Dean et al. 2003). The spectrum of the Cosmic X-ray background can be described by a broken power-law distribution (Gehrels 1992) as given in Eq. (2):

$$\frac{dN_{\text{CXB}}}{dE} = \begin{cases} 0.54E^{-1.4} & E < 0.02\text{MeV} \\ 0.0117E^{-2.38} & 0.02 \leq E < 0.1\text{MeV} \\ 0.014E^{-2.3} & E \geq 0.1\text{MeV} \end{cases} \quad (2)$$

where the dN_{CXB}/dE is in units of counts $\text{cm}^{-2} \text{s}^{-1} \text{MeV}^{-1} \text{sr}^{-1}$.

3.1.2. Cosmic rays

Cosmic rays in low-Earth orbit consist primarily of two components: primary and secondary cosmic rays. Primary cosmic rays originate from outside the solar system and are predominantly composed of protons. Secondary cosmic rays are the product of interactions between the primary cosmic rays and the Earth's atmosphere. Their energies are relatively lower compared to the primary component, mainly concentrated below GeV. As the primary particles approach the Earth, they are influenced by solar activity modulation (which mainly affects low-energy charged particles below GeV) and the Earth's geomagnetic field.

To enter the geomagnetic field, the charged particles must have a magnetic rigidity greater than the geomagnetic cut-off rigidity. By analyzing the observation data from the Alpha Magnetic Spectrometer (AMS) at different geomagnetic latitudes and observation directions from 1998 to 1999, the energy spectrum of primary cosmic rays in low-Earth orbit was derived (Alcaraz et al. 2000a,b). The spectrum of secondary cosmic ray protons was also obtained through fitting of the AMS observational data. The primary component spectrum was fitted with a cutoff power-law distribution, while the secondary component was fitted with a broken power-law distribution (Mizuno et al. 2004).

3.1.3. SAA

The South Atlantic anomaly (SAA) is centered at 45° west longitude and 30° south latitude, with its overall extent ranging from 15° east longitude to 120° west longitude. In this region, the overall intensity of the Earth's magnetic field is low, approximately half of the normal intensity, resulting in a high flux of radiation from charged particles. To protect the LPD instrument from this intense radiation, it will be shut down when passing through the SAA. However, even after normal power-on, the trapped high energy protons in the SAA region will activate some elements. Some nuclides in the instrument with long half-lives will continue to contribute to the background.

Fig. 6 shows the orbit of the CSS and the proton/electron flux in the South Atlantic anomaly and polar regions (data generated by SPENVIS¹). According to the results, LPD is estimated to pass through the South Atlantic anomaly and the poles approximately 8% of the time in one day.

3.2. LPD massmodel and simulation logic

We conduct in-orbit background response studies using Monte Carlo simulation. The mass model of LPD is created using the Geant4² simulation toolkit, as shown in Fig. 7. This model includes the main materials of the LPD payload while omitting certain details like screws. We utilize Geant4 package version 4.10.07 for mass modeling and simulation. The Livermore models in Geant4 are employed for low-energy electromagnetic processes, and features such as X-ray polarization, Auger electrons, and radioactive decay are enabled. In the simulation of photoelectron tracks, the gas above the chip in the mass model is designated as a sensitive volume. Geant4 is used to simulate and track every step of the interaction between photoelectrons and the gas. Once the simulated track backbone is obtained, each step undergoes a digitization process. This process includes transverse Gaussian diffusion, which is proportional to the square root of the drift distance to the upper surface of the GMCP, and charge multiplication of the GMCP. We meticulously choose parameters for diffusion and multiplication to replicate the characteristics of the real experimental process as closely as possible. Finally, the diffused and multiplied photoelectron track is projected onto each pixel of the Topmetal-L chip to form the track, as depicted in Fig. 8. The track reconstruction algorithm for LPD has been discussed in detail in a previous study (Huang et al. 2021b).

¹ <https://www.spennis.oma.be/>

² <http://geant4.web.cern.ch/>

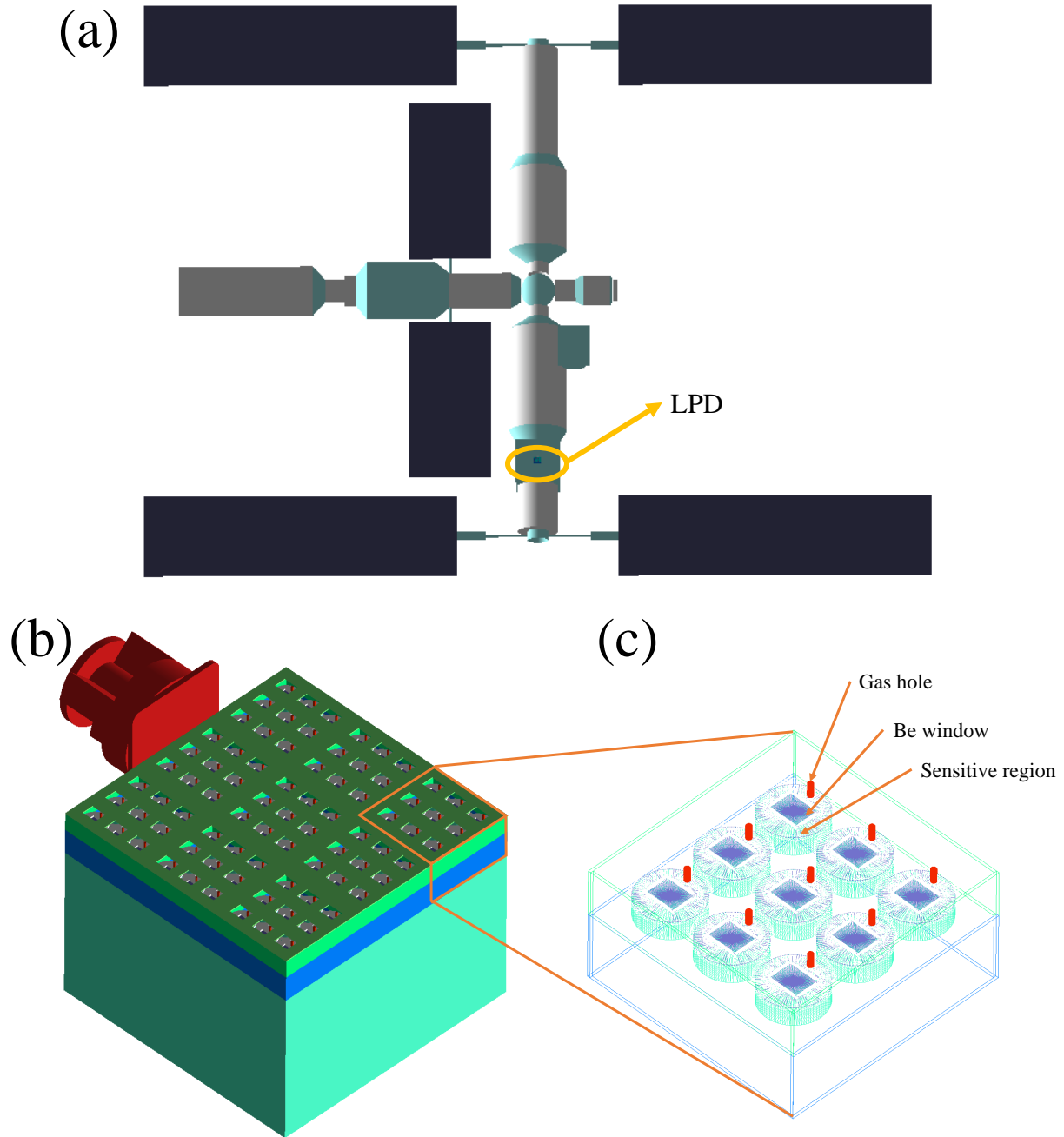


Figure 7. The LPD and CSS mass model was built using Geant4. (a) The simplified model of the CSS features aluminium alloy as its primary construction material. The anticipated position of the LPD is indicated by a yellow circle. (b) The LPD payload, including the mechanical arm adapter (red, main material is aluminium alloy), and the LPD detector array (green). The FoV material is lead glass. (c) The detector module, each of which includes a 3x3 arrangement of gas chambers. The top cover of the gas chamber is made of Kovar alloy, and a copper gas tube traverses through the top cover to establish a connection between the gas and the external environment. The upper end of the copper tube is sealed. The material of the side wall of the gas chamber is aluminum oxide ceramic, which is supported by a ceramic base underneath. At the bottom of the detection gas defines a simplified unperforated GMCP, made of lead glass, with a thickness of 400 micrometers. The upper surface of the GMCP features a layer of plated metal, composed of NiCr alloy, with a thickness of 0.1 micrometers.

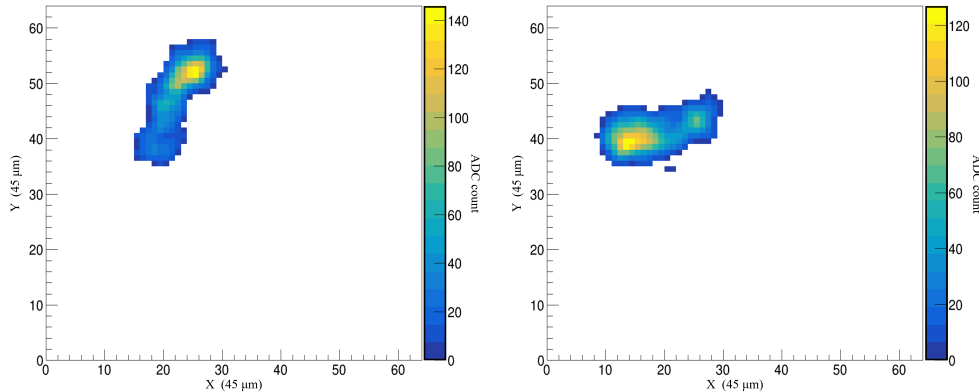


Figure 8. The simulated photoelectron track generated by incident photons with an energy of 6 keV. The detection gas used in the simulation consists of a mixture of Ne (30%) and DME (70%) at a pressure of 0.8 atmosphere. The side length of each square pixel in the image is 45 micrometers. The two endpoints of the track image correspond to Auger electron and Bragg peak (higher energy deposition).

Table 2. Simulation results of energy deposition in the 2-10 keV range at 0 magnetic latitude for different background components, considering the presence or absence of the CSS (unit: counts/cm²/s).

Particle type	Priamry Alpha	Priamry Proton	Priamry Electron	Priamry Positron	Secondary Proton	Secondary Electron	Secondary Positron	CXB
CSS presence	4.77E-03	4.21E-02	3.64E-04	2.20E-05	3.10E-02	4.56E-02	1.69E-01	4.51E-01
CSS absence	5.50E-03	5.42E-02	3.96E-04	2.50E-05	5.01E-02	8.23E-02	2.64E-01	4.57E-01

Table 3. Simulation results of charged particles depositing energy in 2-10 keV at different magnetic latitudes (unit: counts/cm²/s).

Magnetic Latitude	0°	10°	20°	30°	40°	42°
Priamry Alpha	5.50E-03	6.21E-03	8.38E-03	1.39E-02	2.68E-02	3.15E-02
Priamry Proton	5.42E-02	6.04E-02	8.32E-02	1.40E-01	2.89E-01	3.34E-01
Priamry Electron	3.96E-04	4.58E-04	6.82E-04	1.31E-03	3.23E-03	3.96E-03
Priamry Positron	2.50E-05	2.87E-05	4.04E-05	7.58E-05	1.84E-04	2.28E-04
Secondary Proton	5.01E-02	5.15E-02	1.91E-02	1.59E-02	2.02E-02	2.74E-02
Secondary Electron	8.23E-02	8.20E-02	9.56E-03	7.62E-02	7.31E-02	7.24E-02
Secondary Positron	2.64E-01	2.74E-01	1.28E-01	1.25E-01	7.33E-02	7.19E-02
Total	4.57E-01	4.75E-01	2.49E-01	3.72E-01	4.86E-01	5.41E-01

For background simulation, we assume that the Cosmic X-ray Background (CXB) and primary charged particle background have a uniform spherical incidence over a 4 π sr. We also take into account the shielding effect of the Earth, which results in an effective solid angle of 8.3 sr (Cumani et al. 2019) in 400 km orbital altitude. Regarding the secondary charged particle background, it is divided into two components: downward and upward. Each component is assumed to have a uniform spherical incidence over a 2 π sr. At low geomagnetic latitudes, the flux and energy spectra of these two components are approximately equal. The solar modulation potential is set at 650 MV. As for the charged particles in the South Atlantic Anomaly (SAA), we assume that they have a uniform spherical incidence over a 4 π sr.

3.3. Simulation results

The presence of the CSS during the simulation is time-consuming. We initially evaluated whether there is a significant influence from the CSS on the in-orbit background count rate. The simulation results are presented in Table 2. The results of the simulations indicate that considering the presence of the CSS leads to varying degrees of reduction in the count rate of different charged particle backgrounds. This reduction is primarily attributed to the obstruction of

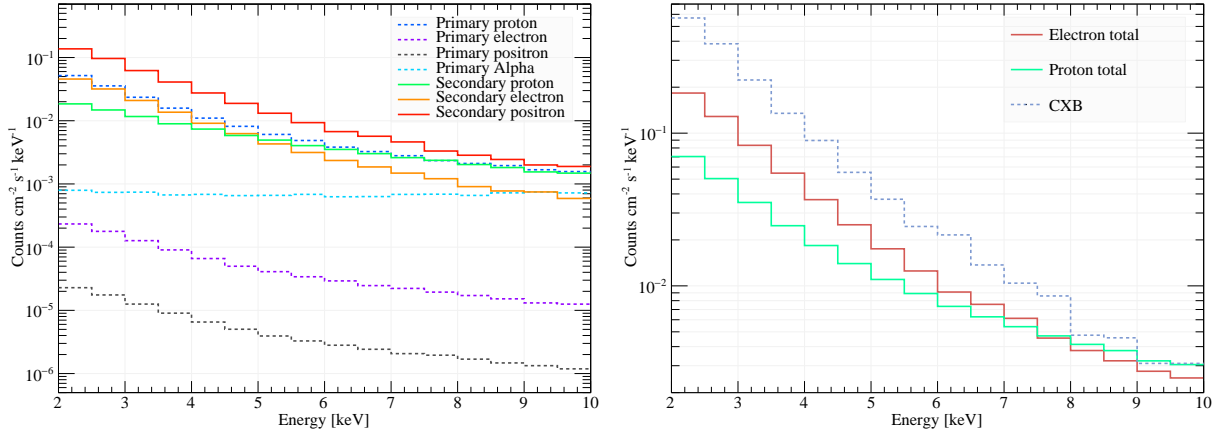


Figure 9. Simulated spectral responses of different background components. Left panel: The energy spectrum response of various charged particle backgrounds. Right panel: The total energy spectrum response of electrons, protons, and CXB background is presented. It should be noted that the category of electrons includes both positrons and electrons.

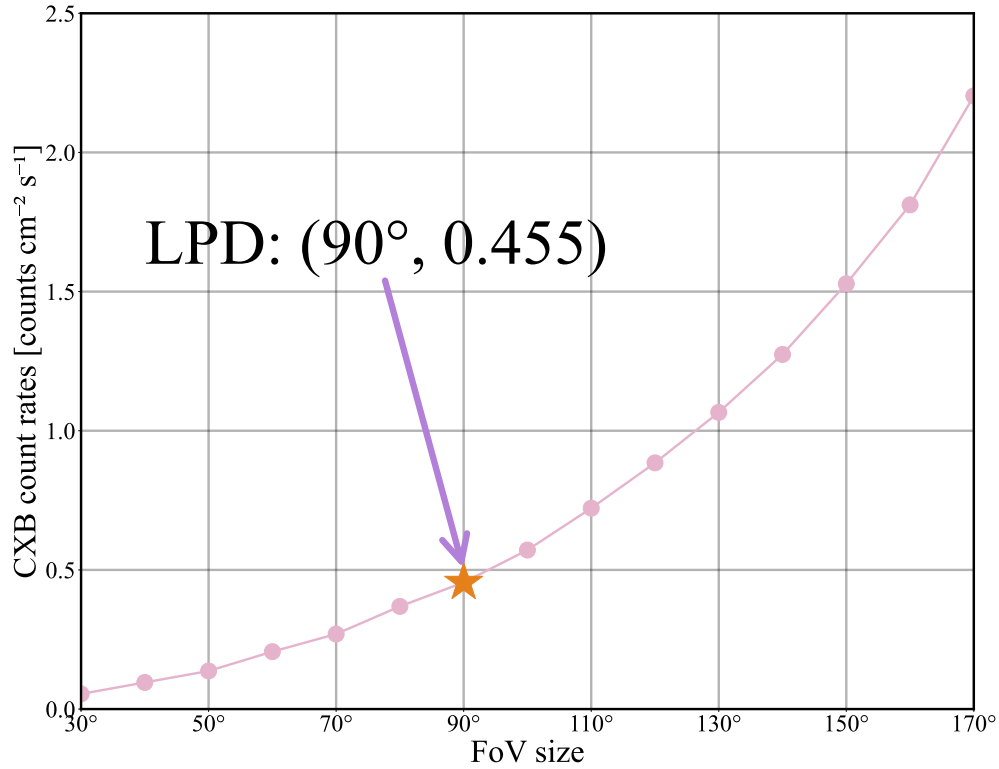


Figure 10. The count rate of CXB changes with the FoV. At a 90° FoV, the count rate is 0.455 count cm⁻²s⁻¹. Please note that in simulating the background response for different FoVs, the obstruction caused by the mechanical arm adapter was not considered. The simulation reveals that, with a 90-degree FoV, the mechanical arm adapter obstructs approximately 2% of low-energy CXB photons, while the scattering of high-energy CXB photons can be deemed negligible.

charged particles by the CSS. Moreover, various shielding materials of the gas chamber, such as ceramics and Kovar alloy, have the capability to block secondary low-energy particles. This may explain why the background count rate does not increase when the presence of the CSS is taken into account. The outcomes also indicate that the count rate of photon background remains predominantly stable, given that photons primarily ingress from the FoV. Due to the yet-to-be-determined relative positions of various payloads on the CSS, more detailed simulations will be undertaken

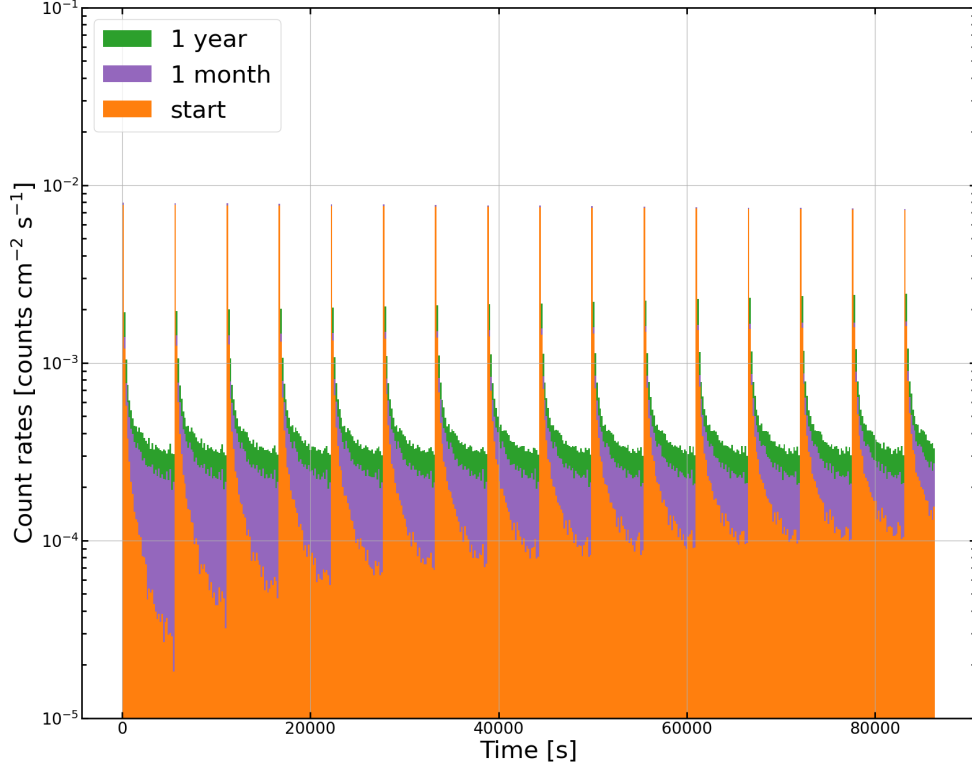


Figure 11. The SAA delayed background changes with time within one day for three different timescales when LPD is in-orbit for beginning, 1 month and 1 year. Each bin in the graph represents 172.8 seconds. Due to the relatively long half-lives of certain elements, the background count rate experience a slight increase with the increase in mission duration.

at a later stage. Additionally, considering the minor impact of charged particles on our results (see Section 3.4), the subsequent detailed simulations in this study will not consider the influence of the CSS.

Fig. 9 illustrates the simulation response of the primary and secondary charged particles, as well as the Cosmic X-ray Background (CXB) in the detector with a 90° FoV. Table 3 provides the simulated responses in the detector for charged particles in the energy range of 2-10 keV at different magnetic latitudes. The results presented in the table indicate that as the geomagnetic latitude increases, the contribution of the primary background becomes more significant, while the overall background response remains relatively stable. These findings are consistent with the results reported in (Huang et al. 2021a).

Furthermore, we conducted simulations to examine the background response for different FoVs. The results demonstrate that the simulated total count rate of charged particles does not change with the FoV of the detector. However, the total count rate of the CXB increases rapidly as the FoV expands within the range of 30 to 170 degrees, as depicted in Fig. 10. It is evident from the figure that the CXB constitutes the largest proportion of the background components under the 90° FoV.

The delayed background caused by protons in the South Atlantic Anomaly (SAA) region decays rapidly once the LPD passes through this area. Fig. 11 illustrates the variation of SAA count rate within one day at different timescales: beginning, 1 month, and 1 year after the LPD is in-orbit. The purpose of this investigation is to examine the cumulative effect of the delayed background. The results indicate that the delayed background in the SAA region can be considered negligible compared to photon background. This may be due to the shielding effect provided by the gas chamber shell. The background primarily originates from materials within the chamber.

3.4. Background rejection for charged particles

Due to the unknown incident direction of X-ray photoelectron tracks, distinguishing X-ray background from GRB X-ray photons presents a challenge. However, there are noticeable differences in the morphological and characteristic parameter distributions between charged particle backgrounds and X-ray photons. This enables the development of background subtraction algorithms for rejecting charged particle backgrounds. Xie et al. (Xie et al. 2021) conducted

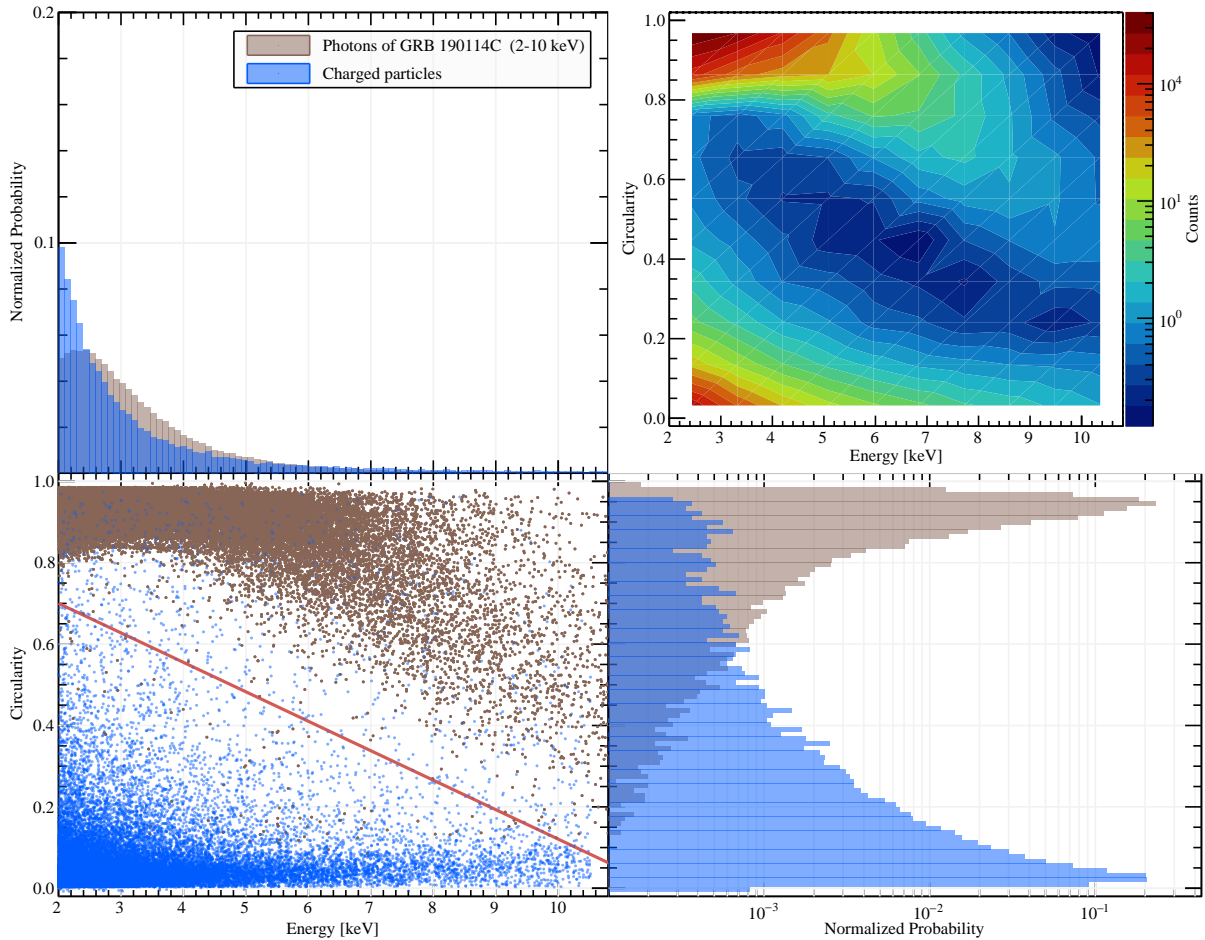


Figure 12. The algorithm of charged particle background screening. The equation of the red straight line in the figure is $y = 0.06x + 0.7$. The background rejection rate after linear cut is 93.22%, and the photon retention rate is 99.94%. The total count rate of charged particle background before the cut is 0.43 counts/cm²/s on average, and after the cut, it reduces to 0.03 counts/cm²/s.

extensive research on the background of IXPE and compared various characteristic parameters of charged particle tracks with those of photoelectron tracks, resulting in a total background rejection efficiency of 75%.

In addition to these methods, a straightforward and efficient approach for rejecting charged particle backgrounds is to compare the circularity (Žunić et al. 2010; Kitaguchi et al. 2018) (a parameter describing the roundness of a track, ranging from 0 to 1, with values closer to 1 indicating a more circular track) and energy deposition distributions of charged particle tracks with those of photoelectron tracks. The rejection efficiency for charged particle backgrounds can exceed 90%, as illustrated in Fig. 12.

4. CATALOGUE OF X-RAY SOURCES AND SIMULATED SKY SURVEY

4.1. Catalogue of X-ray sources

To assess the influence of X-ray sources on gamma-ray burst polarization observations, it is essential to have information regarding the positions, flux, and energy spectra characteristics of each bright X-ray source distributed in space.

MAXI/GSC (Matsuoka et al. 2009) has conducted comprehensive X-ray sky surveys throughout the day and provides daily updates of observational data for X-ray sources on its official website³. The data includes positional coordinates of the X-ray sources and flux variations over time in the energy ranges of 2-4, 4-10, and 10-20 keV. An example of flux

³ <http://maxi.riken.jp/top/slist.html>

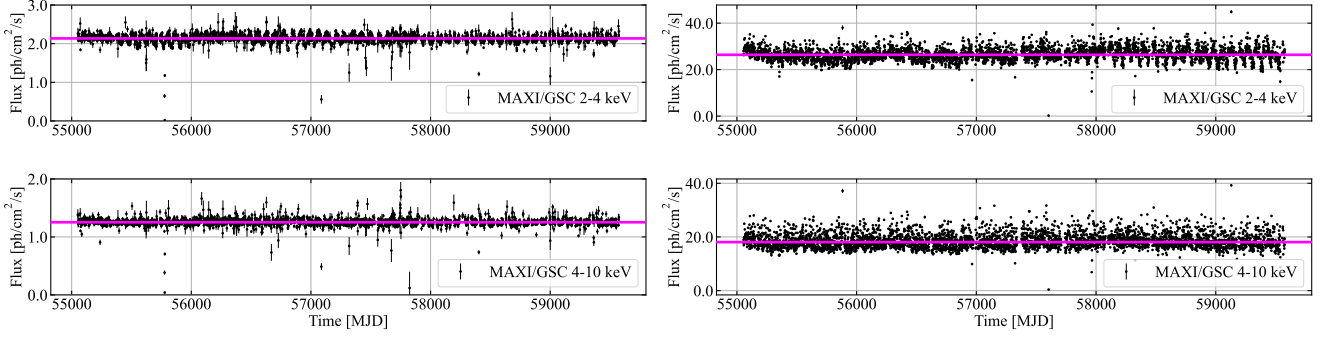


Figure 13. Example of MAXI observation flux data respectively in 2-4 and 4-10 keV. Left panel: Crab; Right panel: Sco X-1. We take the median of the flux as the estimate value for the flux, as shown by the magenta line in the graph.

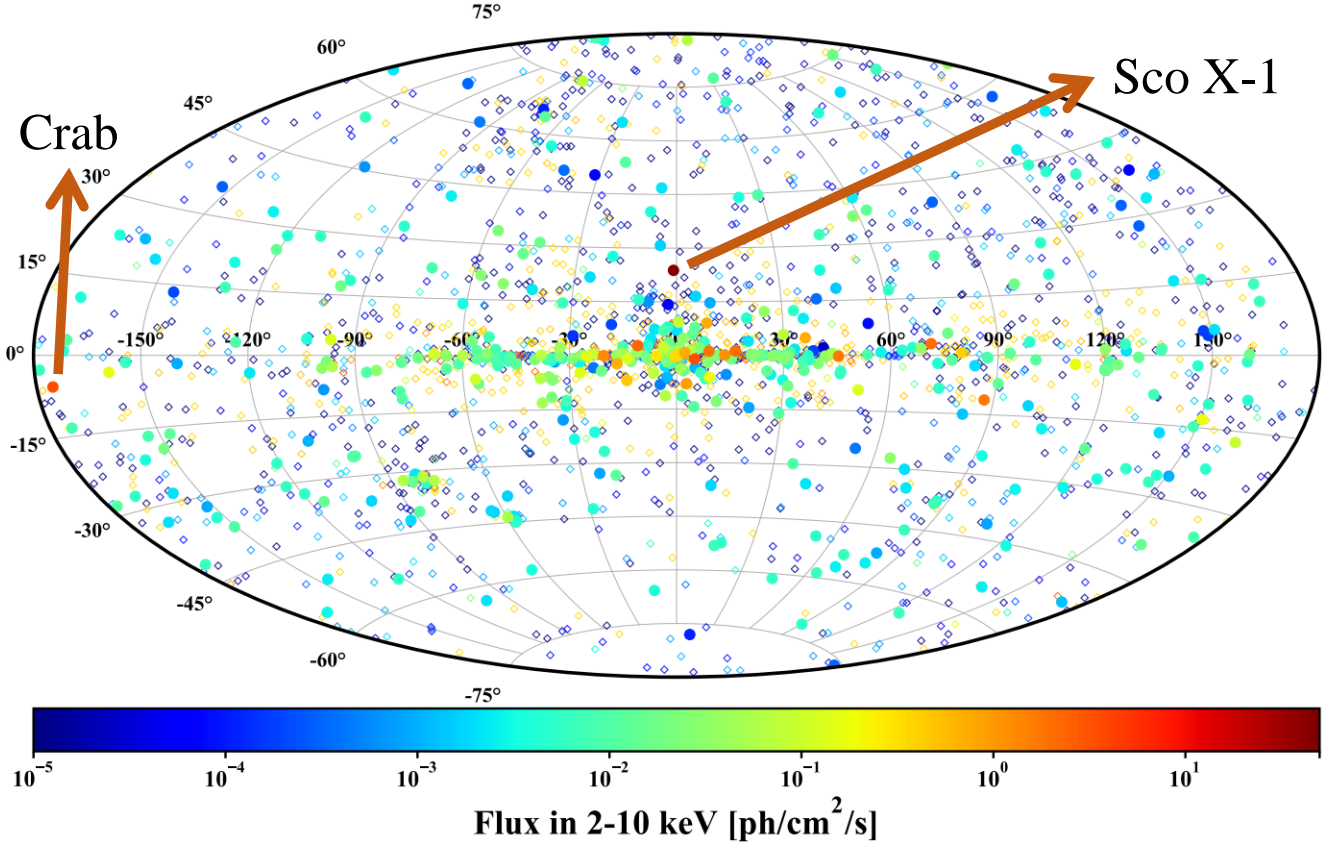


Figure 14. Distribution of the sources on the sky in Galactic coordinates and the flux of each sources in 2-10 keV. The sources detected by MAXI/GSC are indicated by solid circles, and the sources detected just by Swift/BAT are indicated by hollow diamonds. The positions of Crab and Sco X-1 are indicated in the diagram with arrows.

data for Crab and Sco X-1 is shown in Fig. 13. We take the median of the flux as the estimate value for the flux, as shown by the magenta line in the graph.

In 2021, Dagonneau et al. published the Onboard catalogue of known X-ray sources for SVOM/ECLAIRS (Dagonneau et al. 2021). This article performs joint fitting of flux observation data from MAXI/GSC and Swift/BAT (14-195 keV) (Barthelmy et al. 2005) using single power law or broken power law models. The best-fitting spectral models and parameters for each X-ray source in MAXI/GSC and Swift/BAT are obtained. The fitting parameters for each source

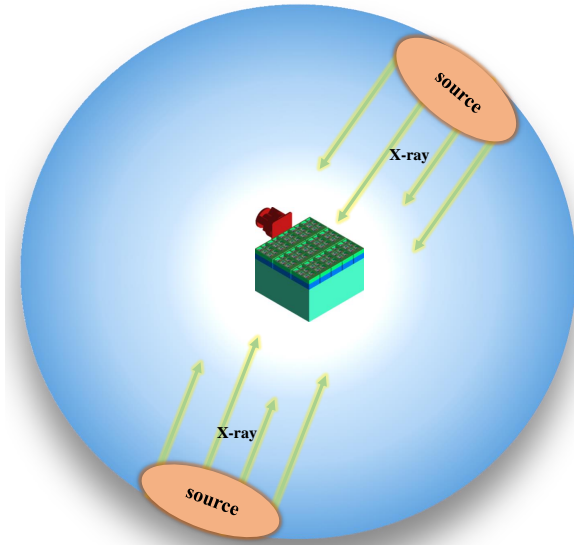


Figure 15. Illustration of the setup for the incident X-ray sources, with the LPD positioned at the center of the sphere. In the simulation of X-ray sources, they are distributed on the surface of the sphere based on their position coordinate distribution, with emission directions pointing towards the center of the sphere.

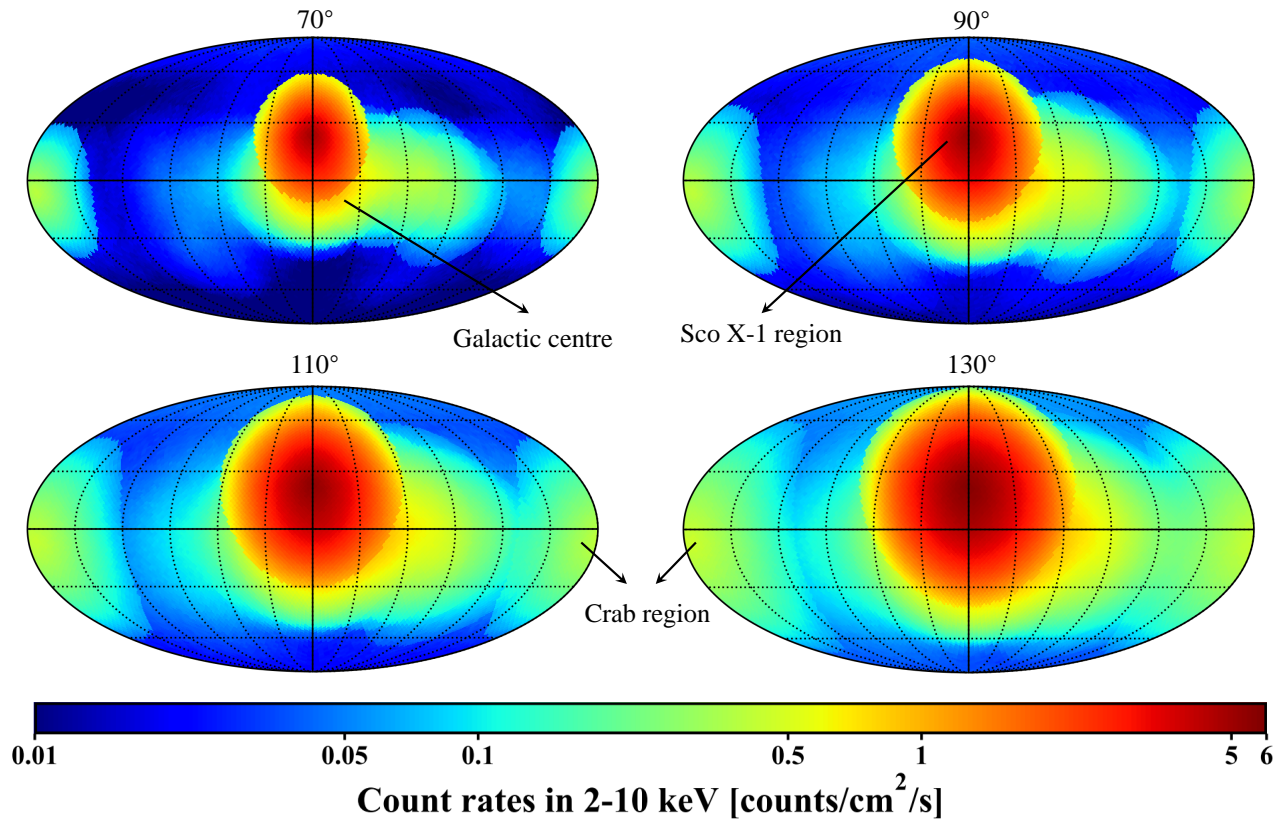


Figure 16. Sky survey simulation maps. The count rate per square centimeter per second from all of the MAXI/GSC sources is depicted based on the pointing direction in the sky in Galactic coordinates (with longitude increasing from left to right). The four maps correspond to the four different FoVs: 70°, 90°, 110°, and 130° (total 12288 pixels).

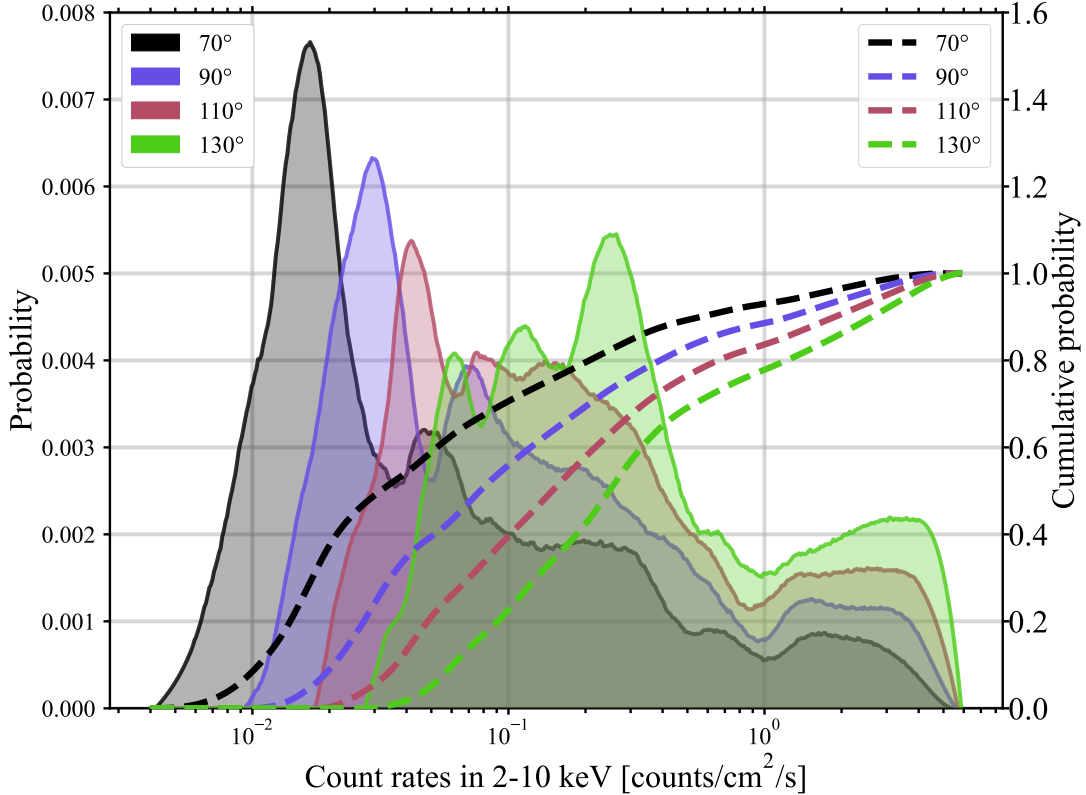


Figure 17. Count rate distributions of sky survey simulation maps under different detector orientations and at four FoVs respectively are 70 degrees, 90 degrees, 110 degrees, and 130 degrees.

are publicly available⁴. From this source catalogue, we utilize all the MAXI/GSC sources and select the Swift/BAT sources that fit well in the 2-10 keV energy range. Fig. 14 shows the sky distribution of the sources in Galactic coordinates and their flux in the 2-10 keV range. It is evident from the figure that the brightest X-ray sources in space in the 2-10 keV range are predominantly located in the galactic plane, except for Crab and Sco X-1.

4.2. Sky survey simulations

Input scripts are generated for each MAXI/GSC source to simulate detections using Geant4. Due to computational resource limitations and the mismatch in observed energy ranges, the sources from the Swift/BAT catalog are not used for simulation. Each script includes the initial position coordinates, emission direction, spectral information, and total flux of the sources. The incident sources are modeled as circular planar sources with sufficiently large areas to cover the entire detector, as illustrated in Fig. 15.

To achieve simulated all-sky surveys of X-ray sources, we vary the pointing direction of the detector. We changed the pointing direction of the detector a total of 12,288 times to generate all-sky survey maps. The simulated maps of bright sources in detectors with different pointing directions, covering FoVs of 70°, 90°, 110°, and 130°, are presented in Fig. 16. The count rate distributions of X-ray sources for different detector orientations are presented in Fig. 17 across the four FoVs.

5. SUMMARY AND DISCUSSION

This paper presents a background simulation study for a new scheme to measure the polarization of GRB prompt emission in soft X-ray range using a gas photoelectric polarization detector with a wide FoV.

Comparing our background simulation results, the CXB constitutes the largest proportion among various background components. The total background count rate is ~ 0.55 count/cm²/s after charged particle rejection at 90° FoV. As the FoV expands, the count rate of the CXB experiences a rapid increase within the FoV range of 30 to 170 degrees.

⁴ <http://cdsarc.u-strasbg.fr/viz-bin/cat/J/A+A/645/A18>

and the probability of bright X-ray sources in the galactic plane as well as the brightest X-ray source, Sco X-1, Crab, entering the FoV increases. In addition, as the FoV expands, the probability of the Sun entering the FoV also increases. The probability of the Sun entering the FoV depends on the specific orbit and the FoV of the detector. For example, for the LPD orbit and a FoV of 90 degrees, the probability of the Sun entering the FoV in a year is approximately 1/5. According to the GOSE's solar X-ray monitoring data⁵, the solar flux in the 2-10 keV range fluctuates between several thousands to tens of thousands photons/cm²/s (Bornmann et al. 1996). Currently, in the laboratory, the LPD detector is capable of tolerating a count rate of around 5000 counts/cm²/s. Observing the Sun is also possible. However, the Sun's surface is quite active, resulting in significant count rate variations. Additionally, the differences in solar flux across different years are substantial. Hence, further research is needed to determine whether it is necessary to power on during the Sun's presence in the FoV. The ability to withstand solar observations is our ultimate design goal due to its immense scientific potential. Recent observations by IXPE and PolarLight of brighter sources, such as Sco X-1, have provided high-confidence polarization data. PolarLight observed a flux-dependent low polarization in the 4-8 keV range and no polarization in the 3-4 keV range for Sco X-1 (Long et al. 2022). Therefore, when these bright sources are located at the edge of the FoV, it is still possible to observe bright gamma-ray bursts with high confidence.

When determining the FoV of the detector, it is crucial to consider not only the background level under different FoVs but also to combine GRB observation simulations (to be discussed in future work) with the expected orbit or effective observation time of the mission.

From the simulation results, it is evident that a wide FoV significantly increases the photon background level of the detector, which is unavoidable when detecting transient sources. However, the flux of most GRB prompt emissions is sufficiently high in soft X-ray range. For example, for GRB190114C, using the spectral data provided on the Swift official website, the flux in the 2-10 keV range is estimated to be approximately 15 photons/cm²/s. With a weight modulation factor of 0.33 and an average background level of 0.55 count/cm²/s, the calculated sensitivity using Eq. (1) for a 20-degree oblique incidence is approximately 7.8% in a 300-second observation. Nonetheless, in order to enhance the detector's performance and achieve greater scientific output, it remains an important research topic for us to optimize the detector and minimize the in-orbit background in the future.

ACKNOWLEDGEMENTS

This work is supported by Department of Physics and GXU-NAOC Center for Astrophysics and Space Sciences, Guangxi University. This work is supported by the National Natural Science Foundation of China (Grant Nos. 12027803, U1731239, 12133003, 12175241, U1938201, U1732266), the Guangxi Science Foundation (Grant Nos. 2018GXNSFGA281007, 2018JJA110048).

REFERENCES

- Agostinelli, S., Allison, J., Amako, K., et al. 2003, Nuclear Instruments and Methods in Physics Research Section A: Accelerators, Spectrometers, Detectors and Associated Equipment, 506, 250, doi: [https://doi.org/10.1016/S0168-9002\(03\)01368-8](https://doi.org/10.1016/S0168-9002(03)01368-8)
- Alcaraz, J., Alpat, B., Ambrosi, G., et al. 2000a, Physics Letters B, 484, 10, doi: [https://doi.org/10.1016/S0370-2693\(00\)00588-8](https://doi.org/10.1016/S0370-2693(00)00588-8)
- . 2000b, Physics Letters B, 490, 27, doi: [10.1016/S0370-2693\(00\)00970-9](https://doi.org/10.1016/S0370-2693(00)00970-9)
- Allison, J., Amako, K., Apostolakis, J., et al. 2006, IEEE Transactions on Nuclear Science, 53, 270, doi: [10.1109/TNS.2006.869826](https://doi.org/10.1109/TNS.2006.869826)
- Atwood, W., Abdo, A. A., Ackermann, M., et al. 2009, The Astrophysical Journal, 697, 1071, doi: [10.1088/0004-637X/697/2/1071](https://doi.org/10.1088/0004-637X/697/2/1071)
- Barthelmy, S. D., Barbier, L. M., Cummings, J. R., et al. 2005, Space Science Reviews, 120, 143, doi: [10.1007/s11214-005-5096-3](https://doi.org/10.1007/s11214-005-5096-3)
- Bornmann, P. L., Speich, D., Hirman, J., et al. 1996, in GOES-8 and Beyond, ed. E. R. Washwell, Vol. 2812, International Society for Optics and Photonics (SPIE), 309 – 319, doi: [10.1117/12.254078](https://doi.org/10.1117/12.254078)
- Burrows, D. N., Hill, J., Nousek, J., et al. 2005, Space science reviews, 120, 165, doi: [10.1007/s11214-005-5097-2](https://doi.org/10.1007/s11214-005-5097-2)
- Bégué, D., & Burgess, J. M. 2016, The Astrophysical Journal, 820, 68, doi: [10.3847/0004-637X/820/1/68](https://doi.org/10.3847/0004-637X/820/1/68)
- Coburn, W., & Boggs, S. E. 2003, nature, 423, 415, doi: [10.1038/nature01612](https://doi.org/10.1038/nature01612)

⁵ <https://solarmonitor.org/>

- Costa, E., Soffitta, P., Bellazzini, R., et al. 2001, *Nature*, 411, 662, doi: [10.1038/35079508](https://doi.org/10.1038/35079508)
- Cumani, P., Hernanz, M., Kiener, J., Tatischeff, V., & Zoglauer, A. 2019, *Experimental Astronomy*, 47, 273, doi: [10.1007/s10686-019-09624-0](https://doi.org/10.1007/s10686-019-09624-0)
- Dagoneau, N., Schanne, S., Rodriguez, J., Atteia, J.-L., & Cordier, B. 2021, *Astronomy & Astrophysics*, 645, A18, doi: [10.1051/0004-6361/202038995](https://doi.org/10.1051/0004-6361/202038995)
- Dean, A., Bird, A., Diallo, N., et al. 2003, *Space Science Reviews*, 105, 285, doi: [10.1023/A:1023995803108](https://doi.org/10.1023/A:1023995803108)
- Fan, Z., Liu, H., Feng, H., et al. 2023, *IEEE Transactions on Nuclear Science*, doi: [10.1109/TNS.2023.3269091](https://doi.org/10.1109/TNS.2023.3269091)
- Feng, H., Liu, H., Liu, S., et al. 2023a, *Nuclear Instruments and Methods in Physics Research Section A: Accelerators, Spectrometers, Detectors and Associated Equipment*, 168499, doi: <https://doi.org/10.1016/j.nima.2023.168499>
- Feng, H.-B., Liu, H.-B., Xie, Y.-J., et al. 2023b, *Journal of Instrumentation*, 18, P08012, doi: [10.1088/1748-0221/18/08/P08012](https://doi.org/10.1088/1748-0221/18/08/P08012)
- Gehrels, N. 1992, *Nuclear Instruments and Methods in Physics Research Section A: Accelerators, Spectrometers, Detectors and Associated Equipment*, 313, 513, doi: [10.1016/0168-9002\(92\)90832-O](https://doi.org/10.1016/0168-9002(92)90832-O)
- Giacconi, R., Gursky, H., Paolini, F. R., & Rossi, B. B. 1962, *Phys. Rev. Lett.*, 9, 439, doi: [10.1103/PhysRevLett.9.439](https://doi.org/10.1103/PhysRevLett.9.439)
- Giacconi, R., Rosati, P., Tozzi, P., et al. 2001, *The Astrophysical Journal*, 551, 624, doi: [10.1086/320222](https://doi.org/10.1086/320222)
- Gill, R., & Granot, J. 2021, *Monthly Notices of the Royal Astronomical Society*, 504, 1939, doi: [10.1093/mnras/stab1013](https://doi.org/10.1093/mnras/stab1013)
- Gill, R., Granot, J., & Kumar, P. 2020, *Monthly Notices of the Royal Astronomical Society*, 491, 3343, doi: [10.1093/mnras/stz2976](https://doi.org/10.1093/mnras/stz2976)
- Gill, R., Kole, M., & Granot, J. 2021, *Galaxies*, 9, doi: [10.3390/galaxies9040082](https://doi.org/10.3390/galaxies9040082)
- Götz, D., Covino, S., Fernández-Soto, A., Laurent, P., & Bošnjak, Ž. 2013, *Monthly Notices of the Royal Astronomical Society*, 431, 3550, doi: [10.1093/mnras/stt439](https://doi.org/10.1093/mnras/stt439)
- Granot, J., & Königl, A. 2003, *The Astrophysical Journal*, 594, L83, doi: [10.1086/378733](https://doi.org/10.1086/378733)
- Huang, J., Feng, H., Li, H., et al. 2021a, *The Astrophysical Journal*, 909, 104, doi: [10.3847/1538-4357/abdd2f](https://doi.org/10.3847/1538-4357/abdd2f)
- Huang, X.-F., Liu, H.-B., Zhang, J., et al. 2021b, *Nuclear Science and Techniques*, 32, 67, doi: [10.1007/s41365-021-00903-0](https://doi.org/10.1007/s41365-021-00903-0)
- Hulsman, J. 2020, in *Space Telescopes and Instrumentation 2020: Ultraviolet to Gamma Ray*, Vol. 11444, SPIE, 474–488, doi: [10.1117/12.2559374](https://doi.org/10.1117/12.2559374)
- Kalemci, E., Boggs, S. E., Kouveliotou, C., Finger, M., & Baring, M. G. 2007, *The Astrophysical Journal Supplement Series*, 169, 75, doi: [10.1086/510676](https://doi.org/10.1086/510676)
- Kitaguchi, T., Black, K., Enoto, T., et al. 2018, *Nuclear Instruments and Methods in Physics Research Section A: Accelerators, Spectrometers, Detectors and Associated Equipment*, 880, 188, doi: [10.1016/j.nima.2017.10.070](https://doi.org/10.1016/j.nima.2017.10.070)
- Kumar, P., & Zhang, B. 2015, *Physics Reports*, 561, 1, doi: <https://doi.org/10.1016/j.physrep.2014.09.008>
- Lazzati, D., Rossi, E., Ghisellini, G., & Rees, M. J. 2004, *Monthly Notices of the Royal Astronomical Society*, 347, L1, doi: [10.1111/j.1365-2966.2004.07387.x](https://doi.org/10.1111/j.1365-2966.2004.07387.x)
- Li, Z., Feng, H., Huang, X., et al. 2021, *Nuclear Instruments and Methods in Physics Research Section A: Accelerators, Spectrometers, Detectors and Associated Equipment*, 1008, 165430, doi: [10.1016/j.nima.2021.165430](https://doi.org/10.1016/j.nima.2021.165430)
- Long, X., Feng, H., Li, H., et al. 2022, *The Astrophysical Journal Letters*, 924, L13, doi: [10.3847/2041-8213/ac4673](https://doi.org/10.3847/2041-8213/ac4673)
- Lowell, A. W., Boggs, S. E., Chiu, C., et al. 2017, *The Astrophysical Journal*, 848, 119, doi: [10.3847/1538-4357/aa8ccb](https://doi.org/10.3847/1538-4357/aa8ccb)
- Lundman, C., Pe'er, A., & Ryde, F. 2012, *Monthly Notices of the Royal Astronomical Society*, 428, 2430, doi: [10.1093/mnras/sts219](https://doi.org/10.1093/mnras/sts219)
- . 2014, *Monthly Notices of the Royal Astronomical Society*, 440, 3292, doi: [10.1093/mnras/stu457](https://doi.org/10.1093/mnras/stu457)
- Lundman, C., Vurm, I., & Beloborodov, A. M. 2018, *The Astrophysical Journal*, 856, 145, doi: [10.3847/1538-4357/aab3e8](https://doi.org/10.3847/1538-4357/aab3e8)
- Matsuoka, M., Kawasaki, K., Ueno, S., et al. 2009, *Publications of the Astronomical Society of Japan*, 61, 999, doi: [10.1093/pasj/61.5.999](https://doi.org/10.1093/pasj/61.5.999)
- McConnell, M. L., Baring, M., Bloser, P., et al. 2021, in *UV, X-Ray, and Gamma-Ray Space Instrumentation for Astronomy XXII*, Vol. 11821, International Society for Optics and Photonics, 118210P, doi: [10.1117/12.2594737](https://doi.org/10.1117/12.2594737)
- Mizuno, T., Kamae, T., Godfrey, G., et al. 2004, *The Astrophysical Journal*, 614, 1113, doi: [10.1086/423801](https://doi.org/10.1086/423801)
- Narayan, R., & Kumar, P. 2009, *Monthly Notices of the Royal Astronomical Society: Letters*, 394, L117, doi: [10.1111/j.1745-3933.2009.00624.x](https://doi.org/10.1111/j.1745-3933.2009.00624.x)
- Negro, M., Lalla, N. D., Omodei, N., et al. 2023, *The Astrophysical Journal Letters*, 946, L21, doi: [10.3847/2041-8213/acba17](https://doi.org/10.3847/2041-8213/acba17)

- Produit, N., Bao, T., Batsch, T., et al. 2018, Nuclear Instruments and Methods in Physics Research Section A: Accelerators, Spectrometers, Detectors and Associated Equipment, 877, 259, doi: <https://doi.org/10.1016/j.nima.2017.09.053>
- Rees, M. J., & Meszaros, P. 1994, The Astrophysical Journal, 430, L93, doi: [10.1086/187446](https://doi.org/10.1086/187446)
- Toma, K., Sakamoto, T., Zhang, B., et al. 2009, The Astrophysical Journal, 698, 1042, doi: [10.1088/0004-637X/698/2/1042](https://doi.org/10.1088/0004-637X/698/2/1042)
- Vadawale, S., Chattopadhyay, T., Rao, A., et al. 2015, Astronomy & Astrophysics, 578, A73, doi: [10.1051/0004-6361/201525686](https://doi.org/10.1051/0004-6361/201525686)
- Weisskopf, M. C., Elsner, R. F., & O'Dell, S. L. 2010, in Space Telescopes and Instrumentation 2010: Ultraviolet to Gamma Ray, Vol. 7732, SPIE, 98–102, doi: [10.1117/12.857357](https://doi.org/10.1117/12.857357)
- Xie, F., Ferrazzoli, R., Soffitta, P., et al. 2021, Astroparticle Physics, 128, 102566, doi: [10.1016/j.astropartphys.2021.102566](https://doi.org/10.1016/j.astropartphys.2021.102566)
- Xie, Y., Liu, H., Feng, H., et al. 2023, Experimental Astronomy, doi: [10.1007/s10686-023-09905-9](https://doi.org/10.1007/s10686-023-09905-9)
- Yonetoku, D., Murakami, T., Gunji, S., et al. 2012, The Astrophysical Journal Letters, 758, L1, doi: [10.1088/2041-8205/758/1/L1](https://doi.org/10.1088/2041-8205/758/1/L1)
- Zalamea, I., & Beloborodov, A. M. 2011, Monthly Notices of the Royal Astronomical Society, 410, 2302, doi: [10.1111/j.1365-2966.2010.17600.x](https://doi.org/10.1111/j.1365-2966.2010.17600.x)
- Zhang, B., & Mészáros, P. 2002, The Astrophysical Journal, 581, 1236, doi: [10.1086/344338](https://doi.org/10.1086/344338)
- Zhang, S.-N., Kole, M., Bao, T.-W., et al. 2019, Nature Astronomy, 3, 258, doi: [10.1038/s41550-018-0664-0](https://doi.org/10.1038/s41550-018-0664-0)
- Žunić, J., Hirota, K., & Rosin, P. L. 2010, Pattern Recognition, 43, 47, doi: [10.1016/j.patcog.2009.06.017](https://doi.org/10.1016/j.patcog.2009.06.017)